Ultrathin sillenite nanosheets with wide-spectrum response and high photocatalytic oxidation performance

Hao Sun[a,b], Chen Wang[c], Yaning Zhang[a,b], Yunhang Shao[a,b], Gaoming Bian[a,b], Zhenlin Wang[a,b], Chaofeng Chen[a,b], Hongyan Liu[a,b], Shuai Dou[a,b], Jing Xu[d], Ying Zhang[a,b], Yang Lou[a,b], Yongfa Zhu[e], Chengsi Pan[a,b]*

[a] *Key Laboratory of Synthetic and Biological Colloids, Ministry of Education, School of Chemical and Material Engineering, Jiangnan University, Wuxi, Jiangsu, 214122, China.*

[b] *International Joint Research Center for Photoresponsive Molecules and Materials, Jiangnan University, Wuxi, Jiangsu 214122, China.*

[c] Harbin Zhongke Materials Engineering Co., Ltd, Harbin, 150040, China

[d] *School of Food Science and Technology, Jiangnan University, Wuxi, Jiangsu 214122, China*

[e] *Department of Chemistry, Tsinghua University, Beijing 100084, China.*

*To whom the manuscript should be contacted: cspan@jiangnan.edu.cn

S1. Experimental Section

S1.1. Bandgap calculation

The energy levels of the CBM and VBM for nanosheets were estimated according to the flat band potentials. According to the reported literature,[1] the band positions were obtained via the following equations:

$$E_{CB} = E_{fb} + E_{(Ag/AgCl)} - E_0 \qquad (1)$$

$$E_{VB} = E_{CB} + E_g \qquad (2)$$

where E_{fb} is the flat band potential of the nanosheet; E_{CB}, E_{VB} and Eg are the energy levels of CBM, VBM, and the bandgap energy the of nanosheet, respectively; and E(Ag/AgCl) is the standard Ag/AgCl electrode (E=0.210 V vs. NHE). E_0 is the difference between the flat-band potential and conduction band for nanosheets.

S1.2. Fluorescence decay spectrum

The PL decay spectra were measured by using a Fluorescence lifetime spectrometer (Lifespec ll, Edinburgh) equipped with a pulse laser (EPL375). The signals were recorded by using the time-correlated single photon counting (TCSPC) method. The PL decay curves were fitted on software (F980) provided by the instrument, and various τ values are tested to obtain a good fitness. The decay time of the photogenerated carriers is represented as $\bar{\tau}$, which can be calculated by the following equation:

$$\bar{\tau} = \frac{B_1\% \times \tau_1^2 + B_2\% \times \tau_2^2 + B_3\% \times \tau_3^2}{B_1\% \times \tau_1 + B_2\% \times \tau_2 + B_3\% \times \tau_3} \qquad (3)$$

Where B_1 and B_2 and B_3 represent the amplitudes of the fast and slow components, τ_1

and τ_2 and τ_3 represent the time constants. The fitting parameters used for our curves are listed in Table S4.

S1.3. MD simulation

All MD simulations were performed with the Focite module using the Universal force field in the Materials studio (Accelrys Inc).[2] Before the MD simulation, geometric optimization was used to relax the structure of the models. MD simulations were conducted in an NVT ensemble at 493 K using the Nosé thermostat. A time step of 1.0 fs was selected to integrate the motion equation. The Ewald summation method was adopted to account for the long-rang electrostatic interaction with an accuracy of 10^{-4} kcal/mol. The van der Waals interaction was calculated by the atomic basis method with the cut-off of 15.5 Å. The total simulation time was 1000 ps.

The Amorphous Cell module and Build Layers tools in the Materials studio were used to construct the simulation systems. During the simulation, the Bi^{3+} cations are in $[Bi_6O_4(OH)_4]^{6+}$ form, while $[CrO_2]^-$ anions are in $[Cr(OH)_4]^-$ form as reported in the literature. [3,4] The $[Bi_6O_4(OH)_4]^{6+}$, $[Cr(OH)_4]^-$ and OH^- solution contains 4, 18, and 6 molecules of the above each ion and 500 water molecules. The solution is placed on the slab (30 ×30 Å^2) of the (400) surface of α-Bi_2O_3 and γ-Bi_2O_3 along with the z-axis. For α-Bi_2O_3, the slab contains two layers of Bi atoms and two layers of O atoms, while for γ-Bi_2O_3, the slab contains four layers, in each of which Bi and O atoms are mixed with each other. To reduce the calculation time, the lower half of the atoms in the slab was constrained. A vacuum layer of 25 Å was added in the z-direction to eliminate the effect of periodic boundary conditions.

S1.4. Measurements of apparent quantum efficiency (AQE)

The apparent quantum efficiency (AQE) for water oxidation was measured using 300 W Xe lamp (FX300, PerfectLight) with different band-pass filters of 420 nm (FWHM=10 nm). The irradiation area was controlled as 1.0×1.0 cm^2.
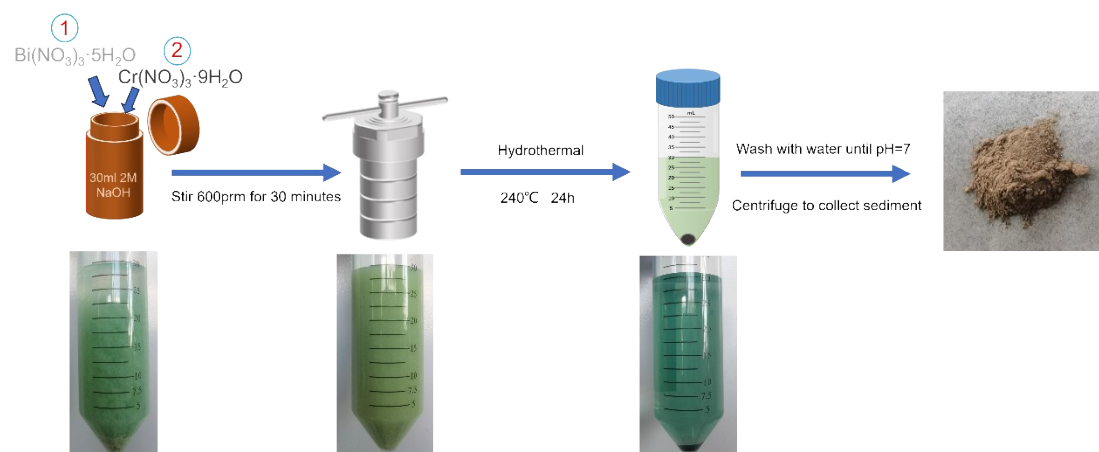The AQE was calculated as follow equation:

$$AQE = \frac{4 \times the\ number\ of\ evolved\ O_2\ molecules}{N} \times 100\% \tag{4}$$
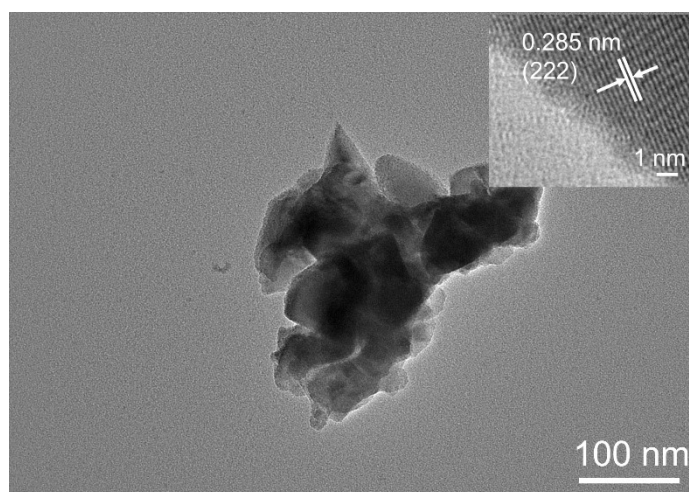
$$N = \frac{E\lambda}{hc} \tag{5}$$

Where N is the quantity of incident photon; E is the incident energy; λ is the

wavelength of light; h is the Planck constant (6.626×10^{-34}); and c is the speed of light

(3×10^8 m/s).

S2. Figures and Tables

**Fig. S1** Schematic illustration for the synthesis of the γ-Bi$_2$O$_3$ nanosheet.

Fig. S2 TEM of γ-Bi$_2$O$_3$ nanoparticles.

Fig. S1 presents TEM images of γ-Bi$_2$O$_3$ nanoparticles. The sample was prepared similarly to the nanosheets but without the addition of chromium salts. The particle sizes range from 300 nm to 500 nm. As depicted in inset HRTEM, the exposed surface of the particles corresponds to the (222) crystallographic plane.

Table S1. XRD refinement parameters for γ-Bi$_2$O$_3$.

Diffractometer	Bruker D8
Radiation	Cu Kα
Range	10-70°
Step	1°/min
Increment	0.02
Chemical formula	Bi$_{12.68}$Cr$_{0.12}$O$_{19.2}$(ICP)
Space group	I23
Lattice constant	a=b=c=10.1751 (3) (Å)
	α=β=γ=90°
Cell Volume (Å^3)	1053.5
R$_{wp}$(%)	9.62
χ^2(R$_{wp}$/R$_{ep}$)	1.83
Atomic coordinates	Bi1 (0.180(7) 0.321(3) 0.481(3)),
	Bi2 (0, 0, 0), Cr (0, 0, 0),
	O1 (0.0280(2) 0.236(4) 0.372(1)),
	O2 (0.124(7) 0.0124(7) 0.124(7)),
	O3 (0.290(2) 0.290(2) 0.290(2))
Occupation	Bi1 (1.02), Bi2 (0.593), Cr (0.119), O1 (1.086), O2 (0.798), O3 (0.737)

Biso	Bi1 (0.51), Bi2 (10.2), Cr (22.8), O1 (0.85), O2 (0.33), O3 (0.73)
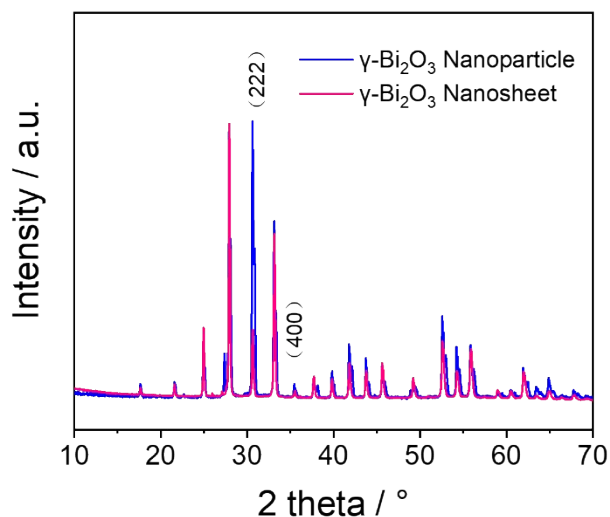
**Fig. S3** (a) XRD patterns of γ-Bi_2O_3 nanoparticles and nanosheets.

XRD reveals distinct changes between nanoparticles and nanosheets. Specifically, the (222) peak intensity for γ-Bi_2O_3 nanoparticles is 9967.7 while a (400) peak intensity is 640.1. In contrast, γ-Bi_2O_3 nanosheets exhibit a diffraction peak intensity of 12470.3 for the (222) plane and 2079.8 for the (400) plane. Therefore, the diffraction peak ratios between the (400) and (222) planes increase for the γ-Bi_2O_3 nanosheets relative to particles. These findings suggest that the nanosheets exhibit growth predominantly along the (400) crystallographic direction.
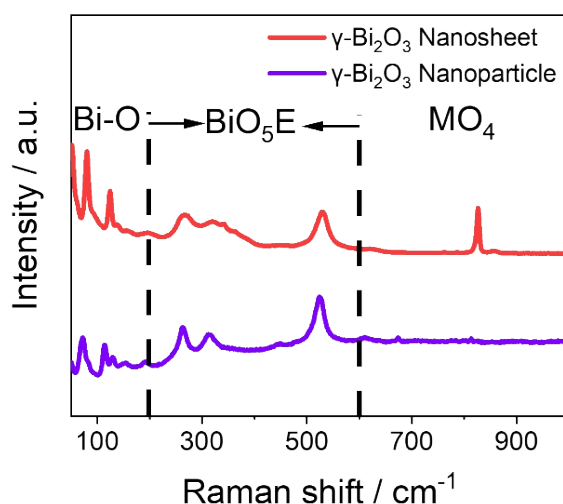
Fig. S4 The Raman spectra of the prepared γ-Bi$_2$O$_3$ nanoparticle and nanosheet.

Fig. S3 compares the Raman spectra of γ-Bi$_2$O$_3$ nanoparticles and nanosheets. The pattern displays peaks located in three regions of 50-200 cm^{-1}, 200-600 cm^{-1}, and 600-900 cm^{-1}, which can be attributed to the vibrations of Bi-O, [BiO$_5$E] octahedra (E represents lone electron pairs), and [MO$_4$] tetrahedra in sillenite, respectively. [5] For Bi-O and [BiO$_5$E] vibrations, γ-Bi$_2$O$_3$ nanosheets exhibit negligible changes relative to their nanoparticles, indicating that the octahedral position is not affected by residual Cr-species. However, a noteworthy change is the emergence of a new peak at ca. 820 cm^{-1} for the γ-Bi$_2$O$_3$ nanosheets. This may be attributed to the symmetrical stretching pattern of Cr-O bonds within MO$_4$ tetrahedra, as reported in previous references, the cations embedded in the tetrahedron strongly affect the electron phonon coupling in sillenite, thereby altering the intensity of the Raman spectrum in the tetrahedron region， indicating that the residual chromium is primarily located in the tetrahedral positions. [6,7]
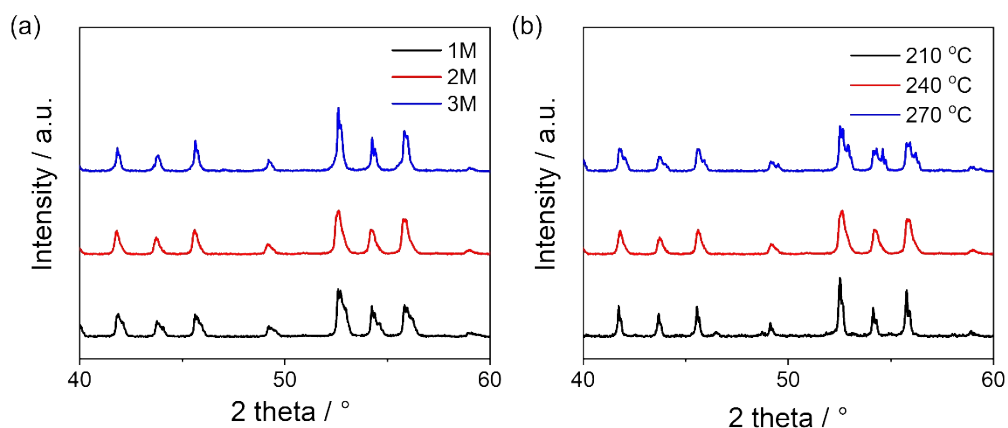
Fig. S5 (a) XRD for γ-Bi$_2$O$_3$ sillenite obtained at different NaOH concentrations. (b) XRD for γ-Bi$_2$O$_3$ sillenite obtained at different temperatures.

Fig. S4a displays XRD patterns obtained at different NaOH concentrations, indicating that a pure phase can only be formed when the NaOH concentration is 2M for γ-Bi$_2$O$_3$ nanosheets. Lower NaOH concentration (1 M) or higher concentration (3 M) result in the generation of impurities. Consequently, it is evident that adjusting the NaOH concentration does not effectively eliminate residual Cr-species. Likewise, the temperature gradient experiment depicted in Fig. S4b yielded similar results, demonstrating that γ-Bi$_2$O$_3$ nanosheets can only be formed at 240 °C. Deviating from this temperature, either by using lower temperature (210 °C) or higher temperature (270 °C), leads to the formation of impurities. Thus, it is evident that altering the temperature does not provide a solution for the removal of residual Cr-species.
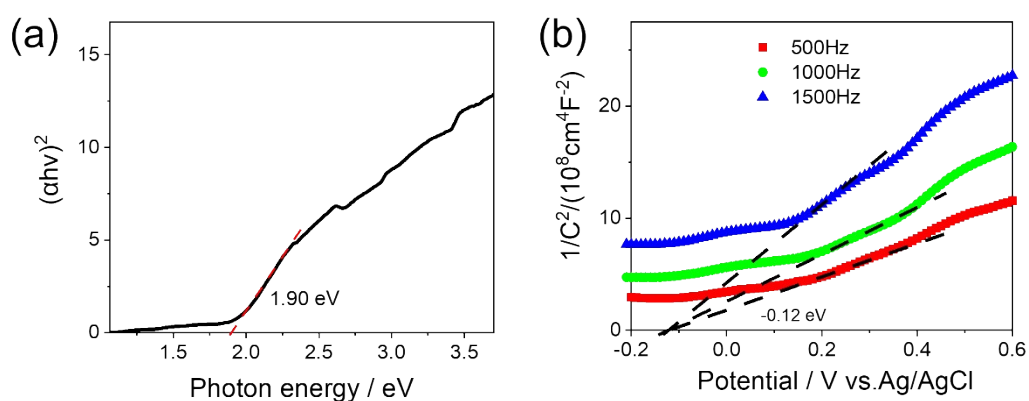
**Fig. S6** Tauc plot (a) and Mott-Schottky (b) of γ-Bi$_2$O$_3$ nanosheet

The Tauc plot shows that the band gap of γ-Bi$_2$O$_3$ nanosheets is 1.90 eV. The Fermi levels are close to the flat band potentials that can be obtained by the Mott-Schottky measurements. The Mott-Schottky curve shows that the flat band potential is -0.12 eV vs. Ag/AgCl. Besides that, a positive slope of the curve indicates that the γ-Bi$_2$O$_3$ nanosheets are n-type semiconductors. Therefore, the valence band is determined to be 2.19 eV for the γ-Bi$_2$O$_3$. The conduction band edge is calculated according to the valence band edge and the bandgap, which is 0.29 eV for the γ-Bi$_2$O$_3$.
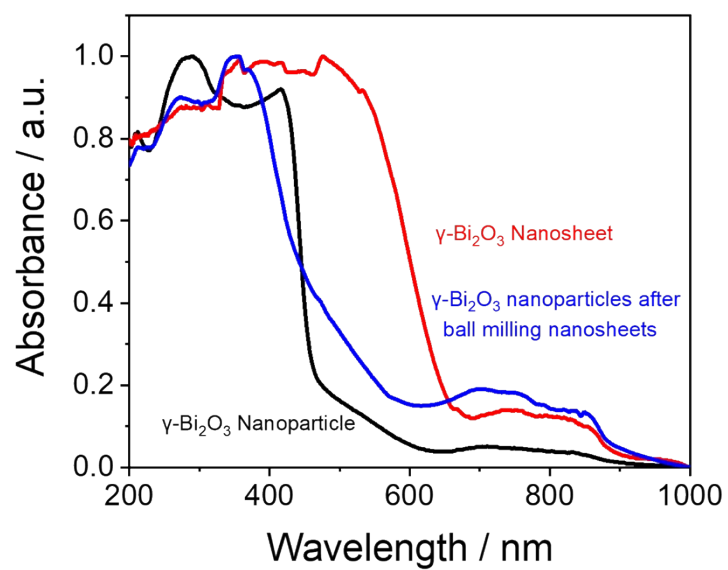
Fig. S7 UV-DRS spectra of γ-Bi$_2$O$_3$ nanosheets, γ-Bi$_2$O$_3$ nanoparticles, and γ-Bi$_2$O$_3$ nanosheet after ball milling (Cr doped nanoparticles).
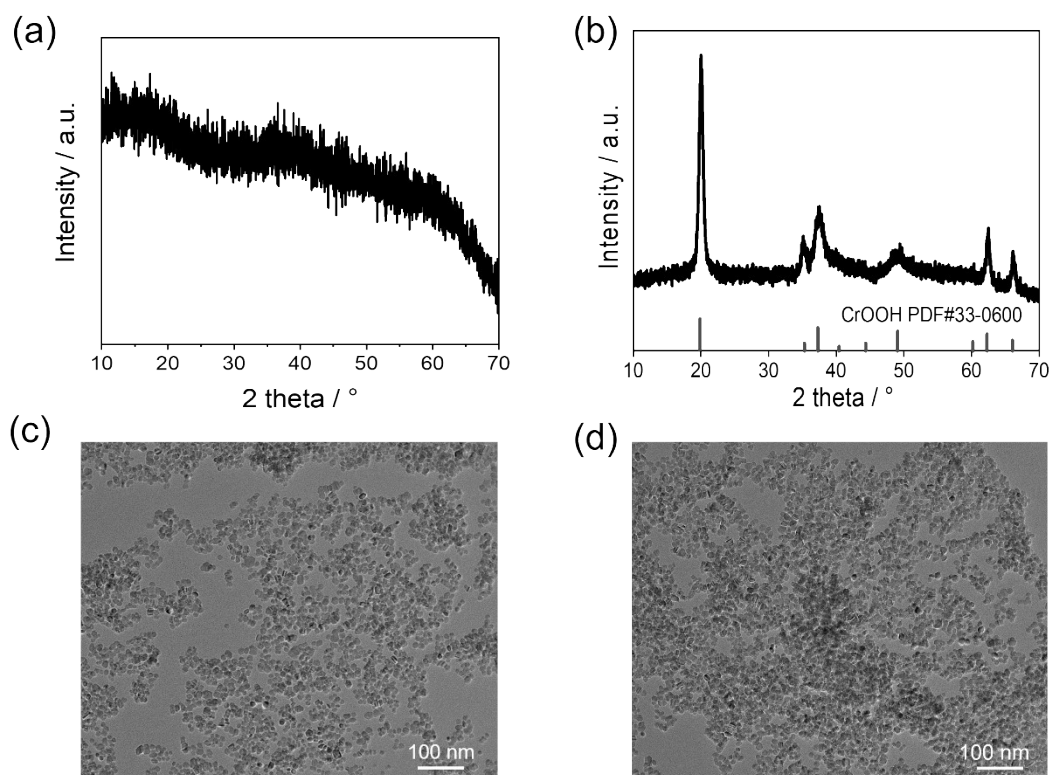
Fig. S8 XRD for CrOOH during the preparation of γ-Bi$_2$O$_3$ nanosheets without Bi-salt addition at 0 h(a) and 24 h(b). TEM for CrOOH during the preparation of γ-Bi$_2$O$_3$ without Bi-salt addition at 0 h(c) and 24 h(d).
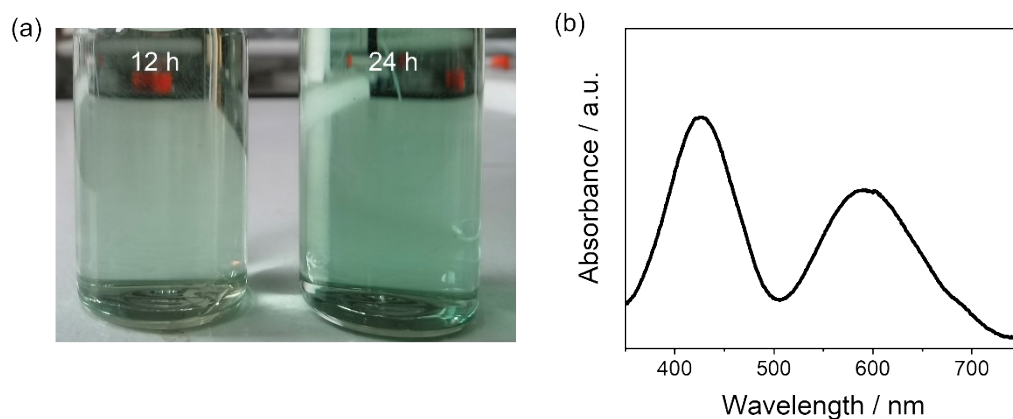
Fig. S9 (a) Photos of supernatant from hydrothermal reaction for 12 h and 24 h. (b) UV absorption spectra of 12 h supernatant.

The UV/Vis absorption spectrum shows two significant bands of nearly equal intensity at 591 nm (yellow to orange-colored) and 420 nm (violet), resulting in the green color of the material. Two bands are well known for isolated $[Cr(OH)_6]^{3-}$.[8]
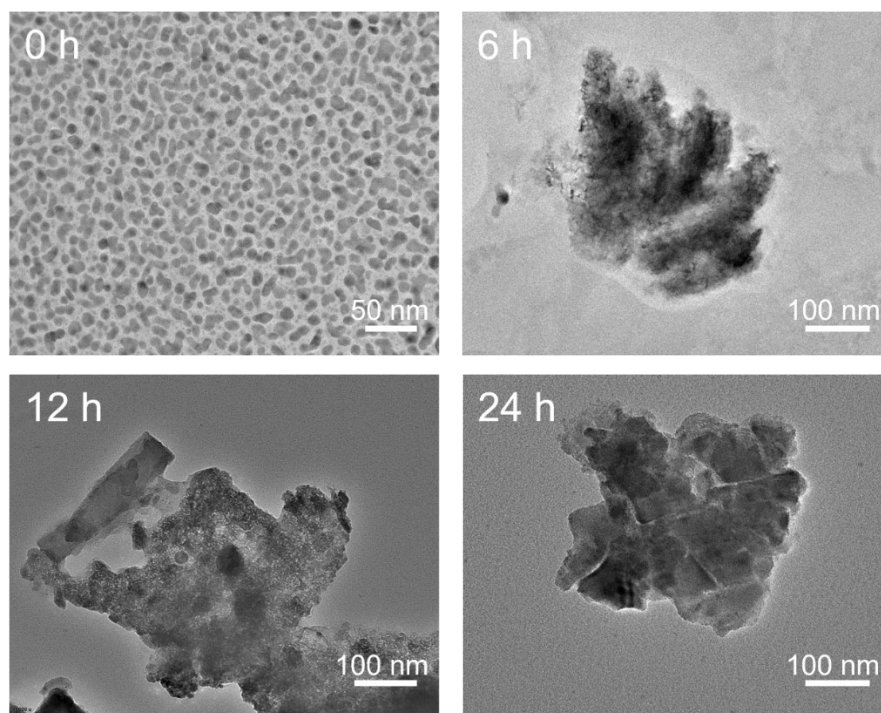
Fig. S10 TEM at different hydrothermal times without adding Cr species.
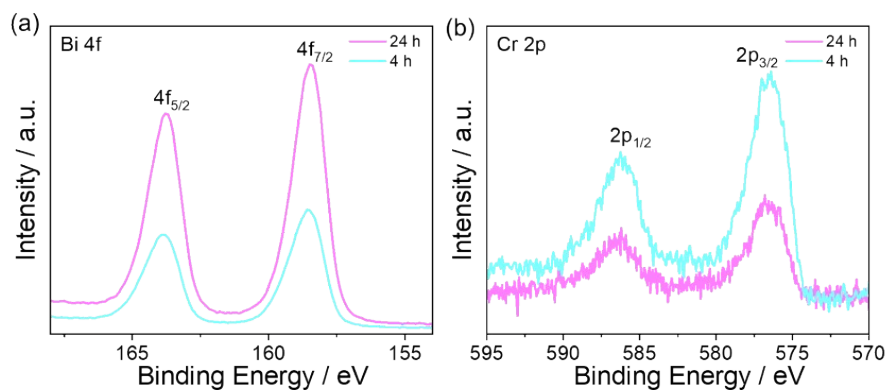
Fig. S11 XPS spectra of Bi 4f (a) Cr 2p (b) in the prepared γ-Bi$_2$O$_3$ nanosheets.

Fig. S8 exhibits XPS narrow scans of Bi 4f and Cr 2p for γ-Bi$_2$O$_3$ nanosheets. The binding energies of Bi 4f observed for γ-Bi$_2$O$_3$ nanosheets are 158.5 eV and 163.7 eV, respectively, classifying them as Bi^{3+}.[9] The binding energies of Cr 2p for γ-Bi$_2$O$_3$ nanosheets are observed at 576.5 eV and 586.5 eV. As reported in literature references, these binding energies can be classified as the 2p3/2 and 2p1/2 peaks of Cr^{3+}.[10,11]
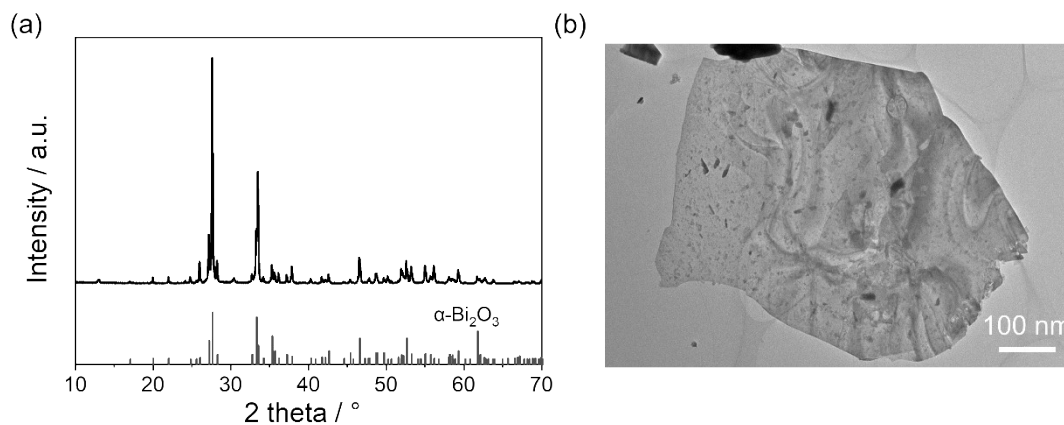
**Fig. S12** XRD(a) and TEM(b) of the prepared α-Bi$_2$O$_3$ nanosheets. The preparation method for α-Bi$_2$O$_3$ nanosheets is similar to that of γ-Bi$_2$O$_3$ nanosheets, except that the hydrothermal temperature is 120°C.

XRD shows that the diffraction peaks of the prepared sample can be attributed to α-Bi$_2$O$_3$ (PDF No. 41-1449). The TEM image of the prepared α-Bi$_2$O$_3$ shows a nanosheet structure with numerous small CrOOH sheets attached onto the surface. This result suggests that if α-Bi$_2$O$_3$ does not transform into γ-Bi$_2$O$_3$, the surface-bound CrOOH will not be removed.
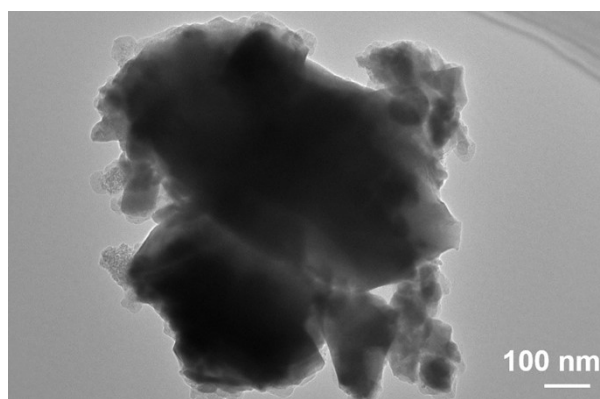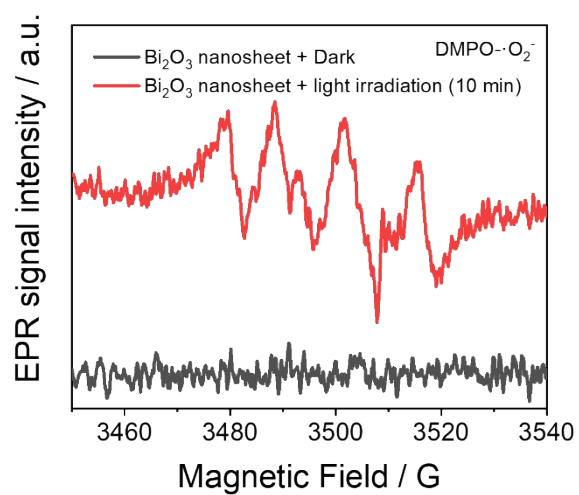
Fig. S13 TEM of γ-Bi$_2$O$_3$ prepared by hydrothermal 48 h with Cr(NO$_3$)$_3$ addition.
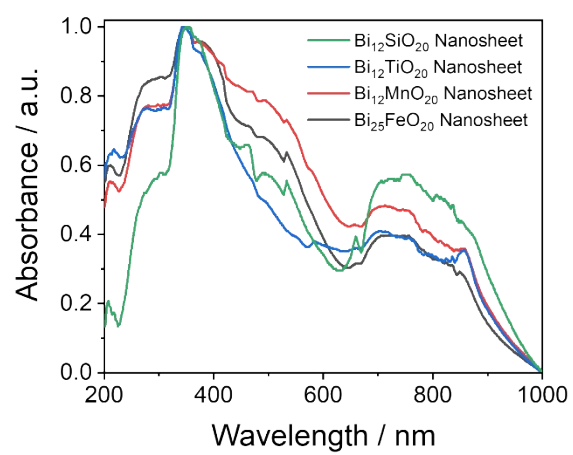
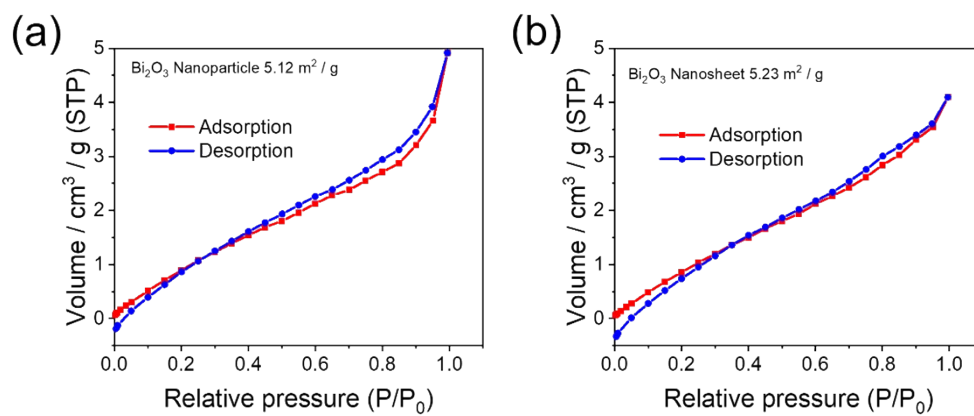**Fig. S14** UV-DRS spectra of the prepared nanosheets.
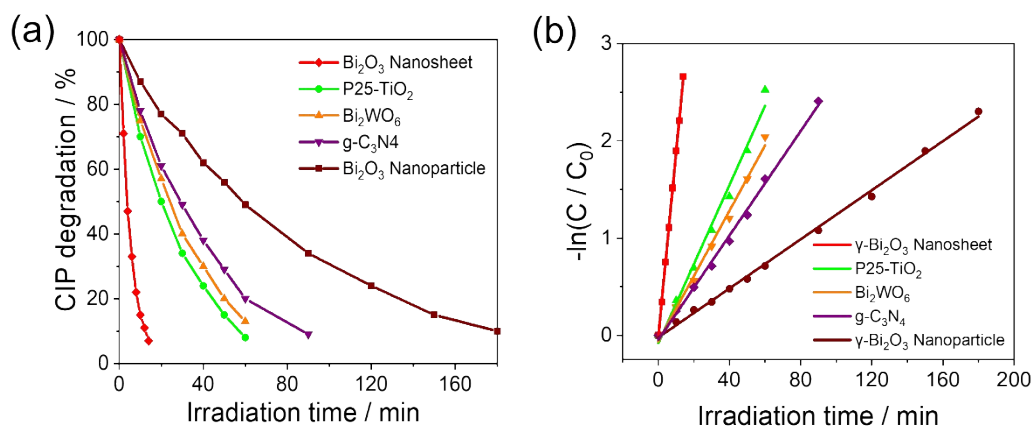
Fig. S15 Photodegradation curves (a) and linear fitting for the concurrent photodegradation curves (b) of CIP degradation by different photocatalysts. (Cat.=1 g/L, CIP=10 ppm, Xe lamp $\lambda > 300$ nm).

.

Fig. 16 EPR spectra of γ-Bi_2O_3 nanosheet under Xe lamp irradiation, superoxide radicals($\cdot O_2^-$) detection in methanol with DMPO as a radical trapper.

(a)

(b)
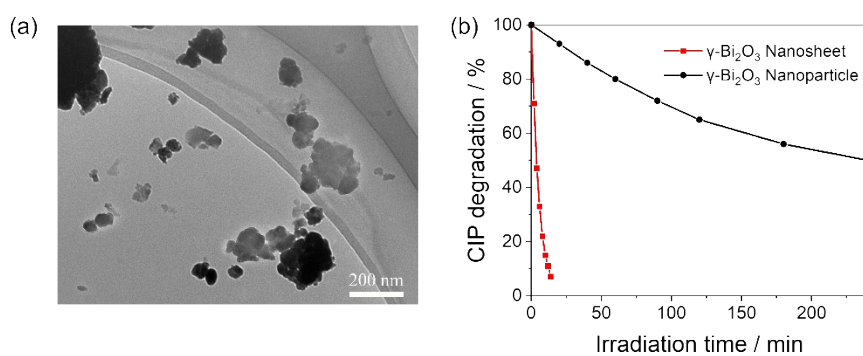
Fig. S17 (a) TEM of γ-Bi$_2$O$_3$ nanoparticles after ball milling nanosheets for 2 h. (1400 rpm, 2 h), (b) Photodegradation of CIP on γ-Bi$_2$O$_3$ nanoparticles derived after ball-milling the nanosheets (1400 rpm, 2 h). Photodegradation of CIP on γ-Bi$_2$O$_3$ nanosheets is shown as controls. (Cat.=1 g/L, CIP=10 ppm, Xe lamp λ > 300 nm).

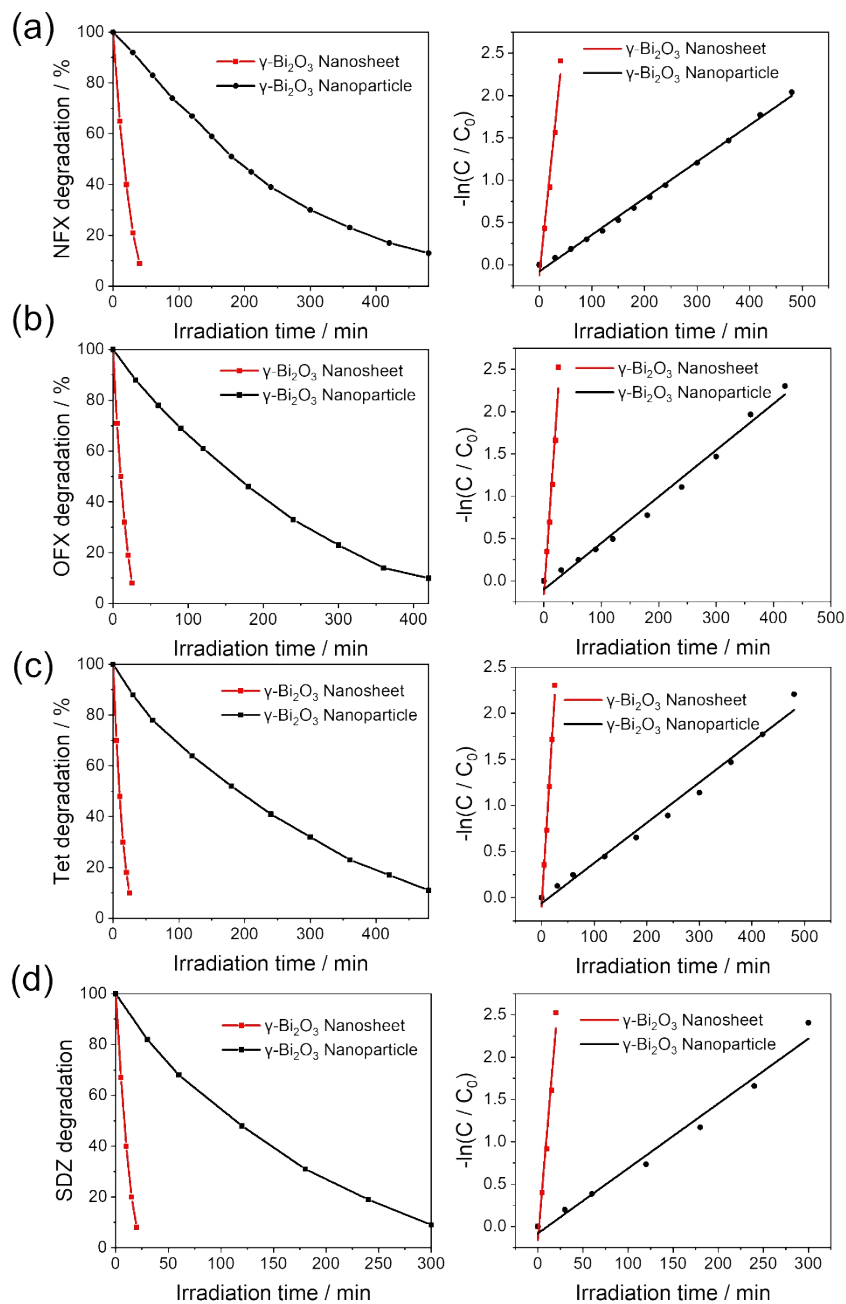**Fig. S18** Isothermal adsorption-desorption curves of prepared γ-Bi_2O_3 nanoparticles and γ-Bi_2O_3 nanosheets.
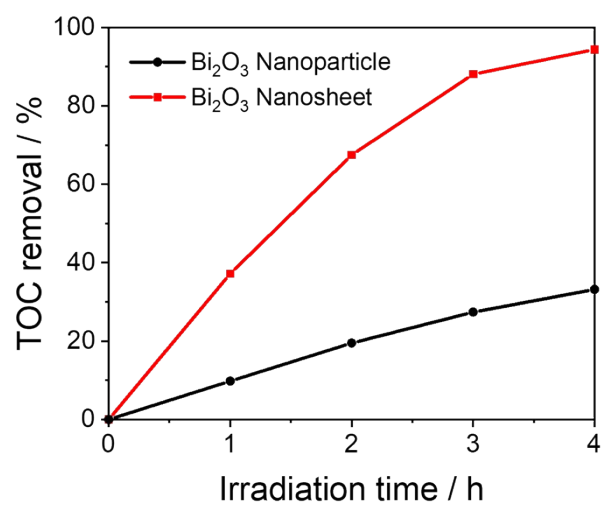
Fig.S19 The TOC removal of γ-Bi_2O_3 nanosheet and γ-Bi_2O_3 nanoparticle for CIP

degradation. (Cat.=1 g/L, CIP=10 ppm, Xe lamp λ > 300 nm).

**Fig. S20** Photodegradation curves and linear fitting for the concurrent photodegradation curves of NFX(a), OFX(b), Tet(c) and SDZ(d) by γ-Bi$_2$O$_3$ nanosheet and γ-Bi$_2$O$_3$ nanoparticle. (Cat. =1g/L, Antibiotics=10 ppm, Xe lamp λ > 300 nm).

Table. S3 Fitting parameters for EIS spectra.

Sample	Rs / Ω	Rct / KΩ	CPE / μF	n
γ-Bi$_2$O$_3$ Nanoparticle-Dark	48.28	16.63	212.61	0.821
γ-Bi$_2$O$_3$ Nanoparticle-Light	37.11	11.73	227.68	0.806
γ-Bi$_2$O$_3$ Nanosheet-Dark	53.43	6.97	204.14	0.845
γ-Bi$_2$O$_3$ Nanosheet-Light	31.47	4.59	254.66	0.780
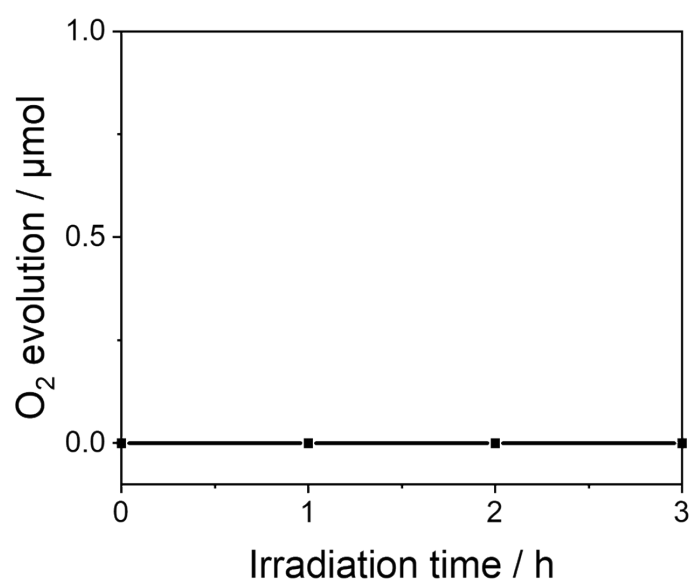
Fig. S21 Time course of photocatalytic oxygen evolution on γ-Bi_2O_3 nanosheet without $AgNO_3$.
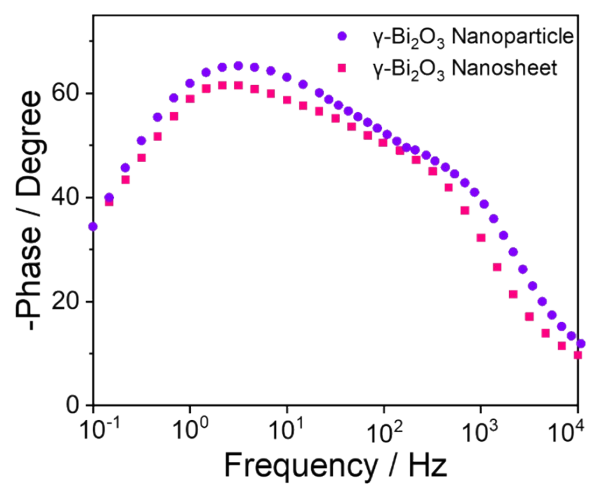
Fig. S22 Bode phase plot of γ-Bi$_2$O$_3$ nanosheets and nanoparticles under illumination.

Table. S4 Fitting parameters for transient PL spectra.

Sample	τ_1 / ns	τ_2 / ns	τ_3 / ns	$B_1\%$	$B_2\%$	$B_3\%$	$\bar{\tau}$ / ns
γ-Bi$_2$O$_3$ Nanoparticle	0.0855	1.1065	5.6526	30.11	39.25	38.18	2.59
γ-Bi$_2$O$_3$ Nanosheet	0.0608	1.1664	5.6468	15.85	30.15	54.00	3.48

References

1   J. Wang, D. Liu, Y. Zhu, S. Zhou and S. Guan, *Appl. Catal*. B.2018, *231*, 251-261.

2   A. Rappe, C. Casewit, K. Colwell, W. Goddard and W. Skiff. *J. Am. Chem. Soc*. 1992, *114*, 10024-10035.

3   S. Bradley, C. Lehr and R. Kydd, *J, Chem. Soc., Dalton Trans.*1993, 2415-2420.

4   E. Sawy, M. Khan and P. Pickup, *Appl. Surf. Sci*. 2016, **364**, 308-314.

5   G. Micheva, T. Nilova, I. Kaurova, Y. Zubavichus and V. Nikolaychik, *J. Cryst. Growth* 2019, **507**, 413-420.

6   R. Panda and A. Pradhan, *Mater. Chem. Phys.* 2002, **78**, 313-317.

7   B. Mihailova, G. Bogachev, V. Marinova and L. Konstantinov, *J Phys Chem Solids*, 1999, **60**, 1829-1834.

8   R. Albrecht, J. Hunger, T. Doert and M. Ruck, *Z Anorg Allg Chem* 2020, **646**, 1130-1137.

9   C. Pan, Z. Wang, Y. Lou, Y. Zhang, Y. Dong and Y. Zhu, *J. Mater. Chem. A.* 2021, **9,** 3616-3627.

10   Z. Xiong and L. Cao, *J. Alloys Compd.* 2019, **773**, 828-837.

11   Y. Chen, G. Mao, Y. Tang, H Wu, G. Wang, L. Zhang and Q. Liu, *Chinese J. Catal.* 2021, **42**, 225-234.